Structural characteristics of Al2O3 ultra-thin films supported on the NiAl(100) substrate from DFTB-aided global optimization

Maxime van den Bossche, Jacek Goniakowski, Claudine Noguera

Journal Name

ARTICLE TYPE

Cite this: DOI: 00.0000/xxxxxxxxxx

Structural characteristics of Al_2O_3 ultra-thin films supported on the NiAl(100) substrate from DFTB-aided global optimization

Maxime Van den Bossche, [ab] Jacek Goniakowski,*[ab] Claudine Noguera,[ab]

Received Date
Accepted Date

DOI: 00.0000/xxxxxxxxxx

Surfaces of aluminum alloys are often coated with ultra-thin alumina films which form by self-limited selective oxidation. Although the presence of such films is of paramount importance in various applications, their structural and stability characteristics remain far from being known. In particular, on the NiAl(100) substrate, the observed structure has been tentatively assigned to a distorted θ-alumina polymorph, but the film stoichiometry, the nature of its surface and interface terminations, as well as the mechanisms that stabilize the θ phase remain unknown. Using a combined tight-binding/DFT genetic algorithm approach, we explicitly demonstrate that ultra-thin θ(100)-type films correspond to the structural ground state of alumina supported on the (2x1)-NiAl(100) substrate. Thus, experimentally observed θ-alumina films correspond to thermodynamic equilibrium, rather than being the result of kinetic effects involved in the alloy oxidation and film growth. They are favoured over other Al_2O_3 phases of dehydrated boehmite, pseudo-$CaIrO_3$, γ, or bixbyite structures, which have recently been identified among the most stable free-standing ultra-thin alumina polymorphs. Moreover, our results prove that film nonstoichiometry can be easily accommodated by the supported θ(100) film structure via an excess or deficiency of oxygen atoms at the very interface with the metal substrate. Dedicated DFT analysis reveals that the oxide-metal interaction at stoichiometric interfaces depends surprisingly little on the composition of the NiAl surface. Conversely, at oxygen-rich/poor interfaces, the number of additional/missing Al-O bonds is directly responsible for their relative stability. Finally the comparison between the experimental and theoretical electronic characteristics (STM and XPS) of supported θ(100)-type films provides clues on the detailed structure of the experimentally observed films.

1 Introduction

Alumina is encountered in many technological fields, such as corrosion protection, gas sensing,[1–3] microelectronics,[4,5] or heterogeneous catalysis.[6–8] These applications may be strongly affected by structural or thickness effects, which are particularly complex when ultra-thin films are formed by self-limited oxidation of aluminum and its alloys. It has, for example, been shown that such alumina films efficiently prevent the adhesion of anti-corrosive galvanic zinc coatings.[9–11] However, despite their importance, the detailed properties of ultra-thin alumina films remain not fully understood.

Indeed, understanding thin film properties requires a precise knowledge of their atomic structure. In the case of alumina this may be challenging due to the considerable structural variety of its bulk polymorphs[12] and is further complicated by finite size effects.[13,14] It has recently been predicted that structures other than corundum are favored when free-standing films are thin enough. They may correspond to cuts of known high energy bulk polymorphs (e.g., γ or θ, the latter being globally stable along the (001) direction at circa 5 - 10 Å thickness), but other unexpected configurations, such as dehydrated boehmite-type, pseudo-$CaIrO_3$-type, or bixbyite were also found among the most stable alumina bilayers.[15]

[a] CNRS, UMR 7588, Institut des Nanosciences de Paris, F-75005 Paris, France.
[b] Sorbonne Université, Institut des Nanosciences de Paris, UMR 7588, INSP, F-75005 Paris, France.
* E-mail: jacek.goniakowski@insp.jussieu.fr

Not surprisingly, supported ultra-thin alumina films may also exhibit entirely new structures, as exemplified by the case of oxidized NiAl(110),[16–18] and $Ni_3Al(111)$[19–21] surfaces, where the observed non-stoichiometric oxide layer about 5 Å thick was first attributed to $\alpha(0001)$ or $\gamma(111)$, or even $\kappa(000\bar{1})$ phases, before it was conclusively shown that its structure is distinct from any bulk alumina polymorph.[18] In contrast, the well ordered crystalline alumina films which were systematically observed at the (100) surfaces of NiAl, CoAl, and FeAl were tentatively assigned to a θ-alumina structure.[22–25]

At the most studied NiAl(100) surface, after oxidation and annealing at high-temperature, (sub)nanometer epitaxial Al_2O_3 films form stripes oriented along [001] or [010] directions of the substrate with a clear (2×1) and (1×2) superstructure pattern.[22,26–30] Based on electron energy loss spectroscopy (EELS) and surface X-ray diffraction measurements, this superstructure was interpreted as a commensurate θ-$Al_2O_3(001)$ one.[22,27] This assignment was also corroborated by scanning tunnelling microscopy (STM) results, which revealed a surface spacing consistent with the lateral size of the θ-Al_2O_3 unit cell.[26,28,29,31,32]

However, since the observed films result from the selective oxidation of an alloy surface, in which Al is preferentially oxidized while the other component does not react with oxygen, the complex effects due to initial alloy oxidation, film growth, and alloy degradation may obviously impact the final film structure.[29,32–36] Despite a long-lasting interest and many experimental studies, the observed structure of alumina films has not yet been the subject of a thorough theoretical investigation. Little is known on their precise composition, their surface and interface terminations, as well as on reasons (thermodynamics vs kinetics) of the formation of the θ phase on the NiAl(100) substrate.

In this context, we have used a combined tight-binding/density functional theory (DFT) genetic algorithm approach to explore the structural diversity of (sub)nanometric alumina films supported on NiAl(100). We explicitly demonstrate that $\theta(100)$-type films correspond to the global energy minima on the (2x1)-NiAl substrate and are favoured over other low energy polymorphs such as dehydrated boehmite, pseudo-$CaIrO_3$, γ, or bixbyite films. In addition, we show that supported $\theta(100)$ structures easily accommodate a non-stoichiometry by an excess or a deficiency of oxygen atoms at the very interface with the metal substrate. Finally, comparison with existing STM and X-ray photoelectron spectroscopy (XPS) allows a detailed structural characterization of the films observed in the experiments.

2 Computational methods and settings

2.1 Density Functional Method

All Density Functional Theory (DFT) calculations are performed with the Vienna Ab initio Simulation Package (VASP) code.[37,38] The dispersion-corrected GGA (optB86-vdW) exchange-correlation functional,[39–41] known to improve the description of adhesion characteristics, is used. The interaction of valence electrons with ionic cores is described within the projector augmented wave (PAW) method.[42,43] The Kohn-Sham orbitals are developed on a plane-wave basis set with a cut-off energy of 400 eV and the self-consistent iterative solution of the electronic Hamiltonian is pursued until energy differences become less than 10^{-6} eV. Atomic charges are estimated with the partition scheme proposed by Bader,[44,45] and atomic configurations are plotted with VESTA.[46]

The NiAl(100) substrate is represented by a three-bilayer-thick slab at the calculated bulk lattice parameters (2.88 Å) and the oxide film is deposited on one side of the support. In all calculations, slabs are separated by at least 10 Å of vacuum and dipole correction is applied. All atomic coordinates are allowed to fully relax until forces get lower than 0.01 eV A^{-1}. We have tested that increasing the NiAl slab thickness does not alter the reported relative stability characteristics. The sampling of the Brillouin zone of the (2×1) surface unit cell is performed with a dense Γ-centred (6×11) Monkhorst-Pack mesh.

Formation energies of stoichiometric alumina films E^{form} are referred to the bulk α phase, i.e.,

$$E^{form} = (E^{tot}_{film/NiAl} - E^{tot}_{NiAl} - nE^{tot}_{\alpha-bulk})/A$$

with $E^{tot}_{film/NiAl}$, E^{tot}_{NiAl}, and $E^{tot}_{\alpha-bulk}$ being the total energies of alumina film with the NiAl support, bare NiAl substrate, and Al_2O_3 formula unit in bulk α phase, respectively. n is the number of formula units in the film unit cell and A is its surface area.

For comparison with experimental data, core level shifts (CLS) are calculated in the well-validated[47,48] complete screening approach, which includes the response of the valence electrons to the creation of a core hole. Screening by the other core-electrons are not taken into account in the present implementation, as it is generally environment-independent and therefore does not significantly influence the CLS.[47] Convergence with respect to the simulation cell size turns out to be crucial and a (8×8)-NiAl(100) one is adopted. Simulations of STM images rely on the Tersoff-Hamann approximation.[49]

2.2 Density Functional Tight Binding method

To reduce the computational workload of the global optimization procedure, we employ an additional, simplified LCAO DFT scheme called density functional tight-binding (DFTB).[50] In its self-consistent-charge (SCC) formulation, DFTB builds on the following approximations: (i) a minimal (but optimized) numerical atomic orbital basis, (ii) one- and two-center approximations for the on- and off-site Hamiltonian matrix elements, (iii) a monopole approximation of the interatomic charge transfer, (iv) short ranged pair potentials for contributions to the total energy other than the electronic energy. Both the short ranged 'repulsive' potentials and the confinement radii for the basis functions and atomic densities are empirical components which need to be fitted

with respect to a DFT training set. In this work, we make use of a prior DFTB parametrization for freestanding Al_2O_3 films,[15] so that only the Ni confinements and Ni-Al and Ni-O repulsions remained to be determined. This is achieved with a training set consisting of the adhesion energies and forces of randomly generated Al_2O_3 thin films on Al- and Ni-terminated NiAl(100) substrates, using the Hotcent[51] and Tango[52] software packages. Additional information regarding the resulting DFTB parametrization is included in the Supporting Information.

2.3 Genetic Algorithm

To locate the most stable supported thin film structures, we employ a global optimization (GO) method referred to as a genetic algorithm (GA),[53,54] as implemented in the Atomic Simulation Environment.[55,56] For a chosen number of Al and O atoms in the supported Al_xO_y film, our GA searches begin by generating an initial set of $2N$ random thin films ($N = x + y$) on a (2×1)-NiAl(100) substrate, followed by relaxation with respect to the atomic positions using DFTB. The following steps are then repeated $2N^2$ times: (i) selecting a genetic operator (cut-and-splice crossover[57] or rattle mutation[57] with resp. 80% and 20% probability), (ii) selecting one (mutation) or two (crossover) "parent" structures from the previously relaxed structures, with a bias towards the most stable ones[58], (iii) applying the operator to the parent structure(s) to create a new "child" structure, which is also subjected to local optimization using DFTB. Each such GA run is furthermore duplicated 20 times, with different random seeds, to maximize the probability of finding all relevant low-lying energy minima. From the resulting set of GA runs, the energies of the 100 most stable structures are recalculated at the DFT level. After this screening, the 30 most stable ones are also locally optimized with DFT.

3 Results

Since direct atomistic modelling of NiAl oxidation, alumina film growth, and associated substrate modifications remain a computational challenge nowadays, our strategy instead aimed at determining thermodynamically stable structures, which could indirectly provide insight into the extent to which the above-mentioned effects impact the observed film structure. Since the experimental film growth is self-limited, neither the thickness of the film nor its stoichiometry are at their thermodynamic equilibrium. In fact, under typical experimental conditions, the latter corresponds rather to a separation of bulk-like α-Al_2O_3 and fcc Ni crystals. For this reason, we carried out explicit structural search for films of several thicknesses and stoichiometries, and considered the possibility of different NiAl terminations.

Following closely the experimental indications, in the global optimization we impose the observed in-plane periodicity of the (2x1)-NiAl(100) substrate, but no structural constraints on the crystalline structure of the alumina film, or on its orientation. In-

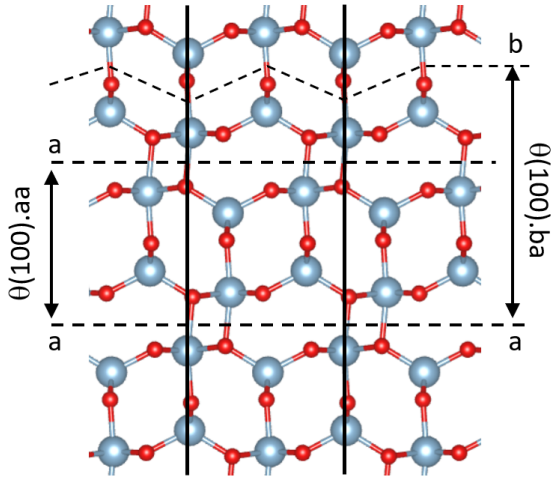

Fig. 1 Side view of the bulk θ alumina structure along the direction perpendicular to the (100) surface. Dashed lines indicate the a and b terminations of the 2ML θ.aa and 3ML θ.ba films. Aluminium and oxygen atoms are represented with blue and red color.

line with the main goal of our study, in the following we first focus on the most stable structures of alumina films (with various thicknesses and stoichiometries) obtained from global optimization on (2x1) and (2x2) Al-terminated NiAl(100) supports. Then, as a complement to these key results, and to gain a broader perspective, we analyze a selection of less stable structures issued from GO, and evaluate the impact of the interaction with NiAl of the most stable free-standing alumina bilayer polymorphs from the literature.

Before reporting our results, we recall that θ-Al_2O_3(100) has recently been predicted to be the most stable structure of free-standing subnanometer alumina films.[15] Although less stable than corundum in the bulk, the particularly low surface energy of its θ.a (1.0 J/m^2) and θ.b (1.8 J/m^2) terminations, Fig. 1, strongly stabilizes films at low thickness. For geometric reasons, films made of an even number of layers (2ML, 4ML, etc.) exhibit two equivalent terminations (either two a or two b, θ.aa or θ.bb films, in the following), while those with an odd number of layers (3ML, 5ML, etc.) expose one a and one b termination (θ.ab films). As a result of the higher surface energy of the b termination, due to the three rather than two broken Al-O bonds (per surface unit cell) and low coordination of the topmost anions, free-standing θ.ab films are somewhat less stable than θ.aa ones.

Another important parameter in the understanding of interface properties is the value of the misfit between the two materials. In the present case, the misfit between the surface lattice parameters of the (2x1)-NiAl(100) substrate (5.76 x 2.88 Å^2) and the relevant ones of the bulk θ-alumina polymorph (5.65 x 2.93 Å^2) is particularly small. Additionally, the 1.9% expansion along the first direction tends to compensate the 1.7% compression along the second one. As a consequence, in the case of ultra-

thin θ-Al_2O_3(100) films, the misfit-induced elastic energy may be as small as 0.1 J m^{-2}, see Sec. 3.2.

3.1 Supported alumina films from Global Optimization

3.1.1 Structural ground states on (2x1)-NiAl(100)

Following the experimental indications, we have first performed an unconstrained global optimization of ultra-thin alumina films on the (2x1) Al-terminated-NiAl(100) substrate (Al-NiAl in the following). To cover the largest possible variety of film and surface/interface configurations, we have considered three alternative thicknesses for the stoichiometric films (Al_4O_6, Al_6O_9, and Al_8O_{12} per (2x1)-NiAl(100) surface unit cell), as well as for the corresponding films with one or two excess oxygen (Al_4O_7, Al_6O_{10}, Al_8O_{13}, and Al_4O_8, Al_6O_{11}, Al_8O_{14}, respectively) or with one missing oxygen atom (Al_4O_5, Al_6O_8, and Al_8O_{11}). The most stable structures issued from GO optimization of the Al_4O_6 and Al_6O_9 series are plotted in Fig. 2. All supported film structures and their total energies are included in the Supporting Information.

The striking finding is that, in all cases, the most stable supported films exhibit a θ alumina structure. Indeed, the film composition Al_4O_6 gives a θ(001) bilayer (2ML), the Al_6O_9 a trilayer (3ML), and the Al_8O_{12} a quadrilayer (4ML). The latter is not shown in Fig. 2 because of its straightforward analogy with the Al_4O_6 bilayer. The supported stoichiometric films are systematically delimited by the most stable θ.a or θ.b terminations. In all cases except Al_4O_7, the most stable θ.a termination is found on the outer surface of the film.

Regarding oxygen-deficient films, we find that they also exhibit a regular θ structure. The oxygen deficiency is systematically accommodated by oxygen vacancies in the alumina layer in contact with the metal substrate. Since this applies to both θ.a and θ.b interfacial terminations of the oxide, the oxygen-deficient films can be considered simply as the corresponding stoichiometric ones, with just one oxygen vacancy at the alumina/NiAl interface.

Similarly, an excess of oxygen does not alter the θ structure, because the additional oxygen atoms are systematically found at the very alumina/NiAl interface in positions which correspond to the prolongation of the alumina lattice. However, in several cases the stoichiometric and O-rich films visibly differ. For example, adding an oxygen atom at the interface to the Al_4O_6 film (a θ.aa bilayer) restructures it entirely into a θ.bb bilayer. This suggests that excess oxygen is much better accommodated by the θ.b termination at the interface. Finally, as it could have been expected, a larger excess of oxygen (an addition of two oxygen atoms per unit cell: Al_4O_8, Al_6O_{11}, and Al_8O_{14} compositions) provokes an oxidation of the topmost Al substrate layer and its incorporation into the alumina film. Interestingly, the resulting configurations, which can be viewed as an O-deficient alumina film (with an additional layer) in contact with the Ni termination of the NiAl substrate, display also the θ(001) structure. We will come back to the

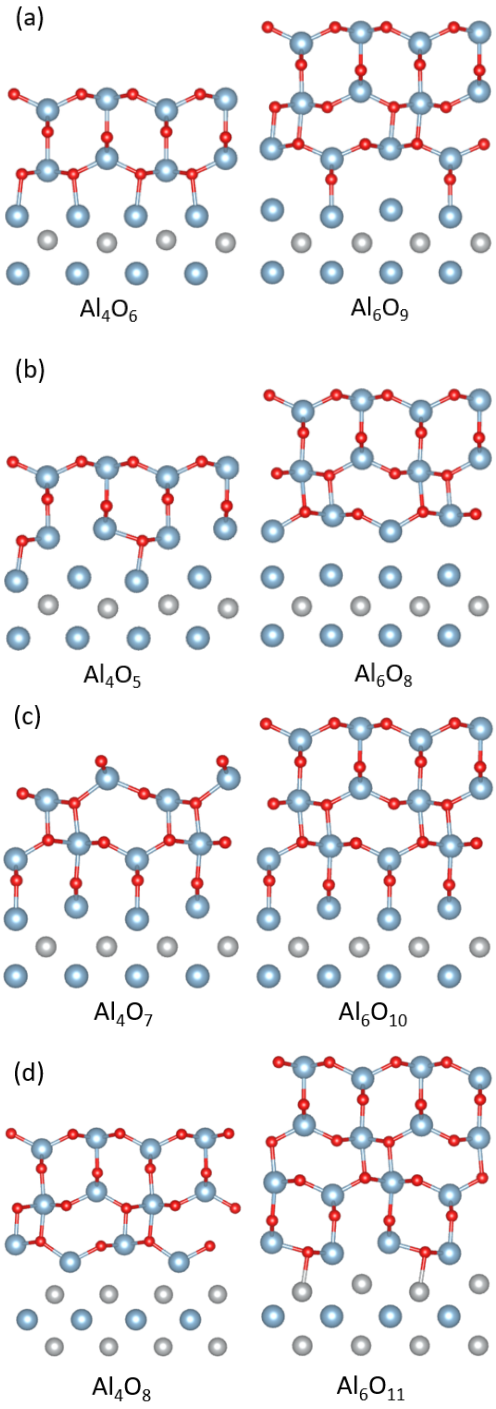

Fig. 2 Atomic structure of the most stable ultra-thin alumina films of varying thickness and stoichiometry supported on the (2x1)-Al-NiAl(100) substrate: stoichiometric (a), O-deficient (b), and O-rich (c-d) films. Nickel, aluminium and oxygen atoms are represented in gray, blue, and red color, respectively.

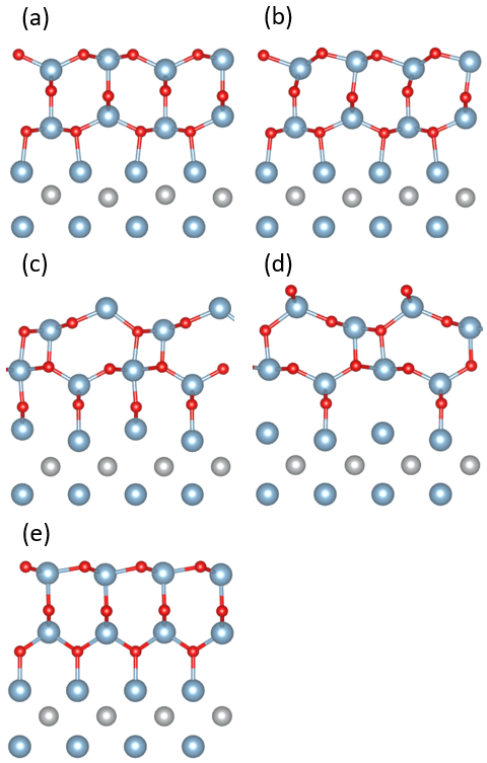

Fig. 3 Atomic structure of selected Al_4O_6 isomers supported on the (2x1)Al-NiAl(100) substrate. Nickel, aluminium and oxygen atoms are represented in gray, blue, and red color, respectively.

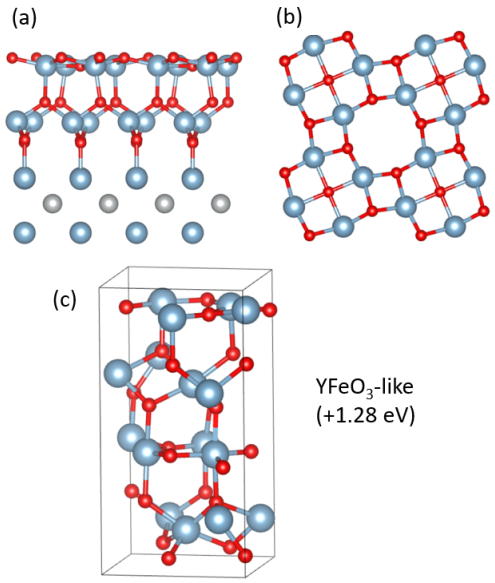

Fig. 4 Atomic structure of the most stable Al_8O_{13} film supported on the (2x2)-Al-NiAl(100) substrate: (a) side view and (b) top view of the surface atomic layer. (c) Structural model and calculated formation energy (eV/fu) of the $YFeO_3$ bulk alumina polymorph relative to α-Al_2O_3.

role played by the particular termination of the NiAl substrate in Sec. 3.2 and in the Discussion.

3.1.2 Less stable structures on (2x1)-NiAl(100)

Beyond the above most stable structures, Fig. 3 report configurations of selected less stable Al_4 O_6 stoichiometric films issued from the GO calculations. The various structural effects illustrated by this particular case provide a robust insight into what may also happen in the other films under consideration. While the majority of the 30 lowest energy isomers display only small alterations in either film structure or in its alignment with respect to the NiAl substrate, the four structures shown in Fig. 3 represent the only qualitatively different configurations. The isomers (b)-(e) are less stable with respect to the ground state θ.aa structure (a) by: 0.65, 0.65, 0.87, and 1.21 eV per unit cell, respectively, which corresponds to an increase of formation energies by: 0.63, 0.63, 0.84, and 1.17 J/m^2, respectively.

Actually, almost all isomers shown in Fig. 3 derive from the ground state structure (a). Configurations (c) and (d) are simply θ.bb bilayers. In the more stable one (c), oxygen atoms are transferred from the outer surface to the interface, which enhances the total number of Al-O bonds but produces a less favourable cationic environments (two-fold coordinated Al in the surface layer). In the absence of such a transfer, in the (d) configuration, one interfacial Al-O bond is lost, which produces a more important destabilization. The configurations (b) and (e) are characterized by three-member Al-O rings in the surface layer. On its own, such a structural change with respect to (a) preserves the number of Al-O bonds, but produces an unfavourable distortion, as seen in (b). A rearrangement of the interfacial layer into an AlO_2 structure with tetrahedraly-coordinated Al cations in (e) enables a better accommodation of this distortion, but is associated with a loss of two Al-O bonds, thus producing the most important film destabilization. Thus, within the experimental constraint of a (2×1)-NiAl(100) unit cell, in a quite substantial range of relative film stability, no isomers are found other than the θ(001) structure and its variants.

3.1.3 Structural ground states on (2x2)-NiAl(100)

Beyond the alumina films on the (2x1)-NiAl(100) substrate, we have extended the unconstrained global optimization over such films on the (2x2)-Al-NiAl(100) support and have considered stoichiometric bilayers (Al_8O_{12} per (2x2)-NiAl(100) surface unit cell), as well as the cases with either excess (Al_8O_{13} and Al_8O_{14}) or missing (Al_8O_{11} and Al_8O_{10}) oxygen atoms.

We find that the lowest energy solutions in the (2x2) cell correspond exactly to those of the same stoichiometry in the (2x1) cell reported above. Also for the Al_8O_{11} film, which has no stoichiometry equivalent in the (2x1) cell, we find a fully analogous θ.aa bilayer with a single oxygen vacancy in the interfacial alumina layer.

The only exception is the most stable Al_8O_{13} film, which also has no equivalent in the (2x1) cell. Its optimal structure, Fig. 4, is

Table 1 The most stable unsupported alumina bilayers from Ref.[15]: parent structure, in-plane lattice parameters, and the formation energy E^{form}. $E^{form}_{strained}$ represents the formation energy of the unsupported film strained as to match the indicated NiAl(100) surface unit cell.

structure	$a \times b$, $\sphericalangle ab$ (Å),(deg)	E^{form} (J/m^2)	$E^{form}_{strained}$ (J/m^2)	NiAl(100)
θ.aa	5.54 x 2.84, 90	2.02	2.14	(2x1)
boehmite	4.89 x 2.97, 90	2.24	2.38	(7x4)
$CaIrO_3$	5.56 x 2.98, 57	2.26	2.72	(7x4)
γ	5.46 x 5.66, 90	2.68	2.84	(2x2)
bixbyite	12.25x12.25, 60	2.74	3.28	(8x4)

1.8 eV (0.85 J/m2) more stable than that derived from the O-rich θ.bb bilayer, Fig. 2(c). The film is composed of an AlO_2 interfacial layer with tetrahedraly coordinated Al cations and an Al-deficient AlO surface layer with a nearly flat rocksalt(100) structure. The film exhibits a clear structural similarity to an AlO_2/AlO bilayer cut out from the $YFeO_3$-like bulk, Fig. 4(c), (1.28 eV/fu less stable than bulk α-alumina), with 1/5 Al atoms removed from the AlO layer. The important outward relaxation around these Al vacancies, visible in Fig. 4(b), allows for a shortening of remaining Al-O bondlengths (less than 2.0 Å) and is thus responsible for the substantial film stabilization.

3.2 The most stable freestanding films on NiAl(100)

In order to broaden the perspective and overcome the constraint related to either the (2x1) or (2x2) surface periodicity imposed during the GO, we have considered the most stable free-standing alumina bilayers found in Ref. 15. They display the dehydrated boehmite(012), the pseudo-$CaIrO_3$(001), the γ_{MG}(001)[59], or bixbyite(111) structures, with formation energies barely greater than the most stable θ(100).aa bilayer, Tab. 1. In the following, we will use a short-hand notation: boehmite, $CaIrO_3$, γ, and bixbyite, respectively.

Since even the relatively small distortions required to fit, e.g., the boehmite or $CaIrO_3$ films into the (2x1)-NiAl cell (5.76 x 2.88 Å) are sufficient to produce their spontaneous transformation into θ.aa bilayers, for each polymorph, we chose a NiAl(100) surface cell which produces an in-plane strain small enough to preserve the initial film structure. As shown in Tab.1 and despite the arbitrary choice of these surface cells which is partly due to computational constraints, one succeeds in obtaining only a small (θ, boehmite, γ) or a moderate ($CaIrO_3$, bixbyite) increase of the unsupported film formation energies.

We find that the energetic preference for the θ.aa structure is preserved also when the films are in contact with whatever (Al or Ni) termination of the NiAl(100) surface, Fig. 5 (top). Indeed, this preference is in all cases larger than the differences of the corresponding elastic energies necessary to match the films with the NiAl substrate, Tab. 1, showing that our conclusion is not biased by the arbitrary choice of coincidence cells in the calcula-

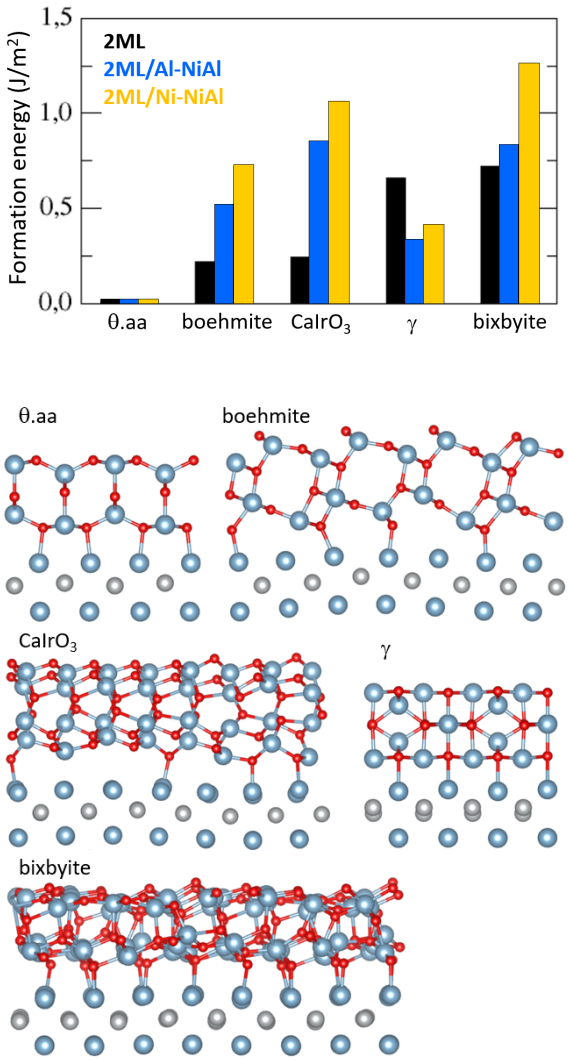

Fig. 5 Top panel: Relative stability of the freestanding, Al-, and Ni-NiAl supported alumina bilayers in θ.aa, boehmite, $CaIrO_3$, γ, and bixbyite structures. Bottom panel: Atomic structures of bilayers supported on the Al-NiAl substrate.

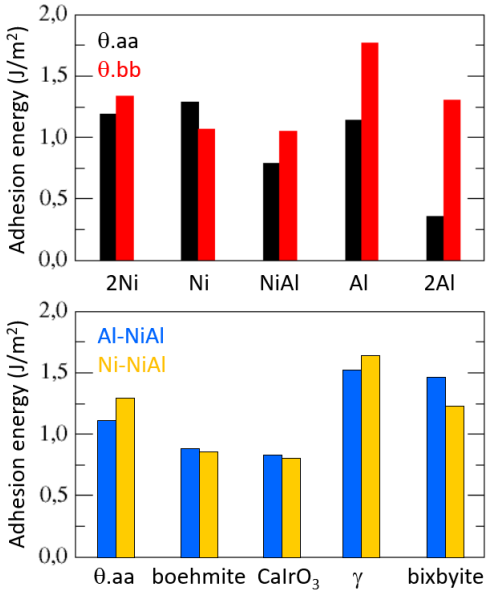

Fig. 6 Adhesion energies of: (top) θ.aa and θ.bb bilayers supported on the NiAl(100) substrate with different surface compositions: Ni bilayer (2Ni), Ni-NiAl (Ni), mixed NiAl bilayer (NiAl), Al-NiAl (Al), Al bilayers (2Al); and (bottom) θ.aa, boehmite, $CaIrO_3$, γ, and bixbyite bilayers in contact with either Al- or Ni-NiAl termination.

tions. Supported boehmite and $CaIrO_3$ bilayers become significantly less stable than supported θ.aa, while the three structures are almost degenerate when free-standing. Conversely, the relative stability of the γ film improves quite visibly. Indeed, the interaction with the substrate reduces the stability difference between θ and γ bilayers to 0.3 J/m^2 only, and makes the supported γ structure the second most stable among the alumina polymorphs under consideration, in agreement with experimental results on nanoscale alumina[13,14]. Although all films happen to be slightly more stable on the Al termination of the substrate, the energy differences between the two NiAl terminations are small, which suggests that the strength of the interfacial interaction between these stoichiometric alumina films and the metal substrate depends little on the precise composition of the NiAl surface. We will return to this point in the Discussion.

4 Discussion

In order to analyze the peculiarities of supported Al_2O_3 films, we will first discuss the nature of adhesion at the alumina/NiAl interface for a wide range of alumina atomic structures and substrate surface compositions. Then, we will formulate a quantitative explanation for the physical mechanisms that are responsible for the stability of configurations found by the GO approach. We will finish by a thorough comparison of our results with the existing experimental data on NiAl(100)-supported epitaxial alumina thin films.

4.1 The nature of the oxide-metal interaction

Figure 6 summarizes the adhesion energies E^{adh} (approximated by the separation energies) between a variety of stoichiometric alumina bilayers and different terminations of the NiAl substrate. One striking feature is the rather weak values of E^{adh}. They all belong to the range 0.5-1.7 J/m^2, typical for non-reactive metal/oxide interfaces between simple, late transition, or noble metals and large gap oxides, while strong adhesion energies would rather reach 2-5 J/m^2.[10] Keeping these numbers in mind, the dependence of E^{adh} on the precise composition of the NiAl surface, Fig. 6 (top), also appears weak. This observation holds for both the θ.aa and θ.bb films, with only two exceptions, namely the most weakly interacting θ.aa/2Al-NiAl interface (E^{adh} = 0.4 J/m^2) and the most adhesive θ.bb/Al-NiAl contact (E^{adh} = 1.7 J/m^2), which will be discussed separately.

These results may seem unexpected because the strong ionicity of NiAl confers a very different electrostatic character to its various surface terminations. On the one hand, the pronounced charges of surface Ni anions and Al cations make the surface layers at Al- and Ni-NiAl(100) positively and negatively charged, respectively. More generally, these terminations display a polar character, which, in semi-conductors and insulators is known to strongly impact surface characteristics.[60] In contrast, while surface atoms also remain charged at the mixed NiAl termination, the surface layers, which consist of an equal number of anions and cations, are globally neutral. Similarly to this last case, at the 2Ni- and 2Al- terminations the excess atoms in the topmost layer become virtually neutral, and so are the corresponding surface layers. In this context, the similar E^{adh} values found on differently charged NiAl terminations suggest that neither substrate polarity nor iono-covalent interfacial Al-O and Ni-O bonds are the principal driving force to interface adhesion. More likely, dispersion, image charge, and polarization forces are at work. In contrast, the interaction is particularly weak and likely uniquely van der Waals-driven at the θ.aa/2Al-NiAl interface (0.4 J/m^2), with an oxide-metal distance larger than 3 Å. Only at the θ.bb/Al-NiAl interface, a low density of short iono-covalent interfacial Al-O bonds actually forms due to the low coordination of the topmost oxygen atom at the b termination and produces a somewhat stronger adhesion (1.7 J/m^2).

Fig. 6 (bottom) displays calculated E^{adh} values for a larger set of stoichiometric oxide bilayers in contact with Al- or Ni-terminated substrates. As previously, for a given oxide structure, adhesion is only weakly dependent on the substrate termination. However, in contrast to the typical picture of weakly-interacting interfaces between metals and wide-gap insulators, our results reveal a substantial dependence of E^{adh} on the interface topology . Indeed, since the θ.aa, γ, and bixbyite bilayers are relatively flat, they enable a good contact with the substrate with a systematically short interfacial distance, Fig. 5. In contrast, the oxide/metal contact is visibly worse for the boehmite and $CaIrO_3$ films, where narrow close contact zones are separated by larger

areas in which the two materials are distant from each other. As expected, the most adhesive interfaces (γ and bixbyite) are characterized by uniformly short interface distances, while the least adhesive ones (boehmite, $CaIrO_3$) exhibit large areas of poor contact. The relatively flat θ.aa bilayer represents a somewhat intermediate case, in which a repulsive interaction makes the interface distance larger than in the γ and bixbyite films, and results in a moderate adhesion strength. Stronger adhesion at the γ/NiAl interface stabilizes the supported γ polymorph but does not make it more stable than the θ one, Fig. 5 (top panel).

4.2 Stability of the θ(100) films

We now focus more precisely on the most stable configurations of alumina thin films issued from the global optimization, Fig. 2. Our results demonstrate that in all cases the oxide has the θ structure and that its relevant terminations, whether in contact with vacuum or with the substrate, are the two most stable θ(100) surfaces, namely the θ.a and θ.b terminations. With the help of dedicated DFT calculations, we will scrutinize the origin of such a strong stability of the deposited θ-alumina films as a function of their stoichiometry and the precise composition of the NiAl surface.

The stability of supported stoichiometric films can be estimated from the total interface energy E^{interf}, which is a sum of interface energies of vacuum/oxide and oxide/substrate interfaces. The former is just the surface energy of the film termination in contact with vacuum $E^{surfS}_{Al_2O_3}$, while the latter involves surface energies of the two surfaces in contact at the interface ($E^{surfI}_{Al_2O_3}$ and E^{surf}_{NiAl}) and the interface adhesion energy E^{adh}:

$$E^{interf} = E^{surfS}_{Al_2O_3} + (E^{surfI}_{Al_2O_3} + E^{surf}_{NiAl} - E^{adh}) \quad (1)$$

Comparing the stability of any two configurations thus involves the difference ΔE^{interf} between the total interface energies, which may rely on: (i) the difference of surface energies of the θ.a and θ.b film terminations (θ.a is by 0.8 J/m^2 more stable than the θ.b, Sec. 3), (ii) the difference of surface energies of Al- and Ni- terminations of the NiAl substrate (Al-NiAl is found to be the more stable by 1.0 $\pm$ 1.0 J/m^2, except in Ni-rich environments), and (iii) the difference between the adhesion energies E^{adh} of the two configurations.

For stoichiometric films, the relative stability of θ.aa (even) and θ.ab (odd) configurations, supported on Al- and Ni-NiAl, has been estimated using E^{adh} from Fig. 6 (top). The results are plotted in Fig. 7 (top panels), where the first and second letters refer to the film termination in contact with vacuum and substrate, respectively. We find that the configurations θ.aa/Al and θ.ab/Al have the lowest total interface energies for even and odd numbers of alumina layers, respectively. These findings correspond well to the most stable structures predicted by the GO, Fig. 2. The lowest E^{interf} values are due to: (i) the smallest E^{surf} for the θ.a termination at the outer surface, and (ii) the largest E^{adh}

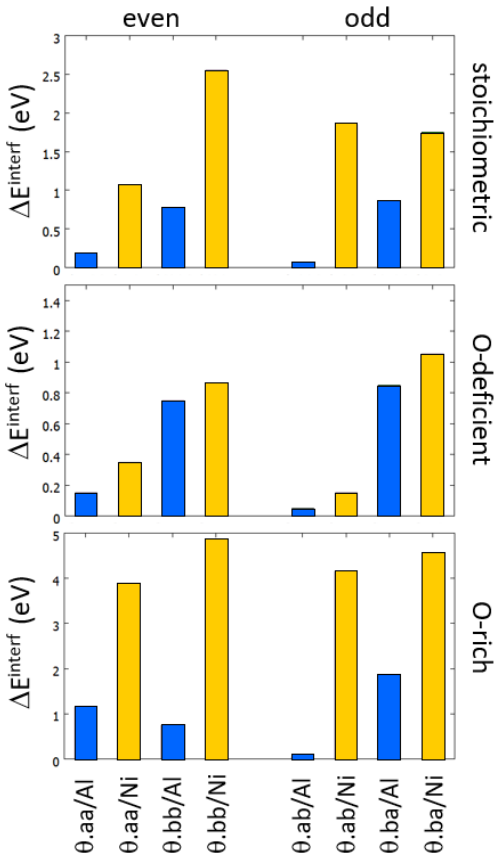

Fig. 7 Relative stability of various configurations of θ-alumina films on NiAl(100). From top to bottom, stoichiometric, O-poor and O-rich alumina films. Films with even and odd number of layers appear on the left and right parts of the histograms, respectively.

Table 2 Characteristics of oxygen extraction and insertion at θ.a and θ.b bilayer interfaces with Al- or Ni-NiAl(100) : oxygen extraction E^{ext}, and insertion E^{ins} energies (eV/unit cell), and the corresponding change of the substrate charge ΔQ_{sub} (e/unit cell).

	O extraction		O insertion	
termination	θ.a	θ.b	θ.a	θ.b
	E^{ext}		E^{ins}	
Al-NiAl	5.4	5.4	-4.8	-5.8
Ni-NiAl	4.7	3.7	-3.0	-3.5
	ΔQ_{sub}		ΔQ_{sub}	
Al-NiAl	+0.08	-0.52	+1.22	+1.31
Ni-NiAl	-1.06	-1.08	+0.87	+0.85

value at the θ.b/Al interface.

Moving now to supported O-deficient or O-rich films, their stability can be estimated from the total interface energy E^{interf} of the corresponding stoichiometric supported film to which is added the energy to extract an oxygen atom E^{ext} or to insert one E^{ins}. The oxygen extraction and insertion energies at the θ/NiAl interfaces estimated by dedicated DFT calculations, Tab. 2, present a well pronounced dependence on both the film structure and the substrate termination.

Oxygen extraction is systematically endothermic ($E^{ext} > 0$) because it requires the breaking of Al-O bonds in the oxide film. Three Al-O bonds have to be broken at the θ.a termination, but only two at θ.b, leading in principle to a smaller energy cost of oxygen extraction from the latter. However, the existence of a iono-covalent interfacial Al-O bond at the *b*/Al-NiAl interface, makes the E^{ext} values at the Al-terminated substrate very similar. We note that at this substrate termination the excess electrons left by the missing oxygen atom are shared between the oxide and substrate Al atoms. In contrast, at the Ni-terminated substrate, they are transferred to the surface Ni atoms ($\Delta Q_{sub} \sim$ -1e). This reduces the cost of oxygen extraction, because the oxide CB is positioned well above the NiAl Fermi level (LDOS in Fig. 8). Thus, for both structural and electronic reasons, the oxygen extraction process is the least endothermic at the θ.b/Ni interface.

Using these E^{ext} values together with E^{interf} of stoichiometric interfaces, we find (Fig. 7, middle panels) that the most stable oxygen-deficient configurations are the θ.aa/Al and θ.ab/Al(Ni), for films with an even or an odd number of layers, respectively, in good agreement with the predictions from the GO, Fig. 2. Their lowest E^{interf} values are principally due to the good stability of the θ.a termination and the smallest E^{ext} for the θ.b/Ni(Al) interfaces. The predicted similar stability of odd θ.ab films on both Al- and Ni-NiAl substrate is enabled by the relatively small surface energy difference between the two substrate terminations.

Oxygen insertion at the θ/NiAl interfaces is systematically exothermic ($E^{ins} < 0$). The most favourable processes take place at interfaces with the Al-terminated substrate where interfacial iono-covalent Al-O bonds are formed, characterized by a substantial electron transfer ($\Delta Q_{sub} \sim$ +1e) towards the inserted oxygen. The insertion is the most exothermic at the θ.b/Al interface where the steric accommodation of the additional oxygen atom requires less structural distortions in the oxide film. In contrast, since interfacial Ni-O bonds formed at interfaces with the Ni-terminated substrate are much weaker, they are associated to a smaller electron transfer and produce a visibly smaller energy gain.

Using these E^{ins} values together with the E^{interf} values of the stoichiometric interfaces, the configurations θ.bb/Al and θ.ab/Al are found to be the most stable, for films with an even or an odd number of layers, respectively, Fig. 7 (bottom panels), in agreement with the GO results, Fig. 2. This is entirely due to the most favourable E^{ins} at the θ.b/Al interface, which is able to compensate the surface energy difference between the θ.b and θ.a film terminations and thus leads to the unique case in which the θ.bb film (with a θ.b-terminated outer surface) is the most favoured.

4.3 Comparison with experiment

Our computational results show that θ films represent the ground state alumina structure on the (2x1)-NiAl(100) substrate. In addition, the fully optimized structures are consistent with the existing tentative assignment of the Bain epitaxy relationship between the face-centered cubic structure of the oxygen-sublattice of the oxide and the body-center cubic structure of the NiAl substrate, i.e., (001) O-sublattice // (001) NiAl surface and [110] O-sublattice // [001]/[010]NiAl.[27–29,31,32] In this way, our results definitively prove that the experimentally observed θ-alumina structure corresponds to the structural ground state, rather than being the results of kinetic effects involved in the alloy oxidation and film growth.

In order to strengthen the link with the existing experimental evidence, we have simulated the STM images of supported θ(100) bilayers, Fig. 8. Experimentally, the oxidized surface can be imaged at low resolution in a wide range of bias voltages without major changes in its general appearance.[26,28,29,32,61] In contrast, the high resolution imaging which reveals the atomic lattice can only be obtained at high negative voltage.[31] Under these conditions, STM images show periodic protrusions every 2.7 $\pm$ 0.1 Å and 5.4 $\pm$ 0.1 Å, separated by trenches with an apparent depth of 1.5 $\pm$ 0.1 Å, Fig. 8 (top)[31]. The simulated STM images, Fig. 8 (bottom), were obtained within the Tersoff-Hamann approximation [49], which uses the integration of the electronic density of states in an energy window determined by the STM bias. As a consequence, LDOS, Fig. 8 (middle), in the corresponding energy window provides directly the essential information on the nature of states which contribute to the image contrast. In agreement with the experimental conditions, the best-resolved simulated STM images are obtained at a large negative bias, of the order of -4 V. This is due to the large offset between the film and the substrate band structures (Fig. 8, middle), which arises from the difference of their surface work functions and is further enhanced

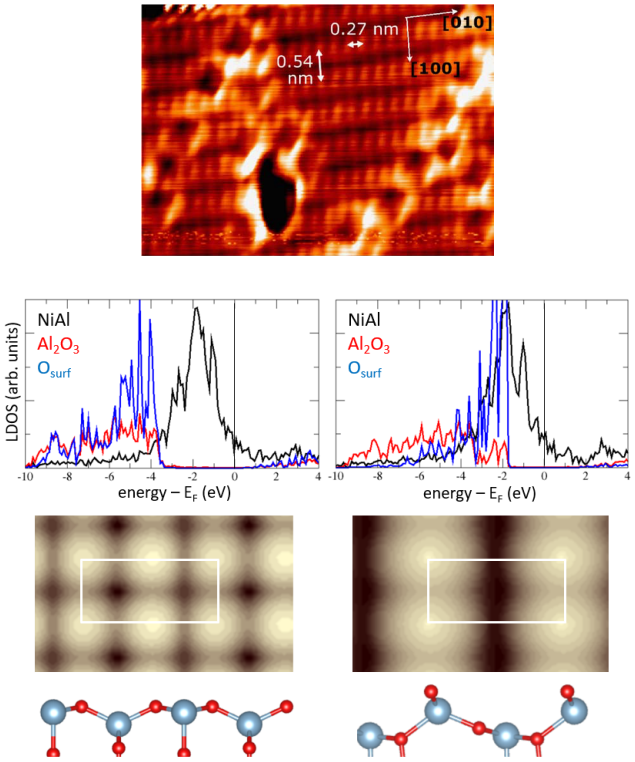

Fig. 8 STM imaging of the θ-alumina/NiAl(100) film. Top: Experimental STM image reprinted from Ref. 31, copyright (2005), with permission from Elsevier. Middle: Density of states projected on the NiAl substrate (black) and the alumina film (red) for the θ.aa/Al-NiAl (left) and θ.bb/Al-NiAl bilayers (right). LDOS of outermost oxygen atoms are explicitly indicated. Bottom: corresponding simulated STM images and side views of the topmost surface atomic layer. The (2×1)-NiAl(100) surface unit cell is indicated.

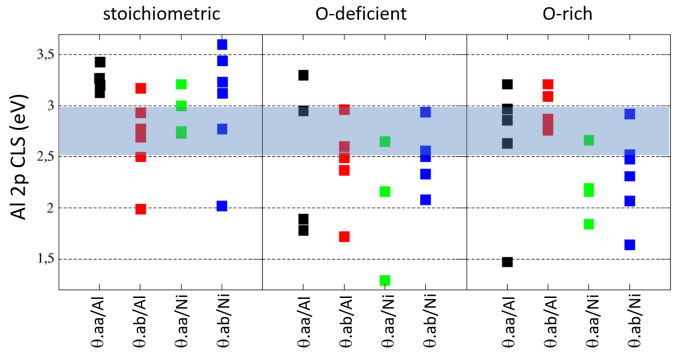

Fig. 9 Al 2p core level shifts (CLS) with respect to a bulk-like reference in the central layer of the NiAl slab for stoichiometric (left), O-deficient (middle), and O-rich (right) 2ML and 3ML alumina films in contact with either Al- or Ni-terminated NiAl substrate. The experimental XPS signature is indicated with the blue stripe.

by the compression of the electron spill-out at the NiAl surface upon the interface formation. At such negative bias the oxide valence band states display mainly an oxygen character and so the STM contrast is dominated by the surface anions. For geometric reasons, a single surface oxygen per (2x1) unit cell is imaged at the θ.b outer surface. It produces an overall rectangular pattern (2.88 × 5.76 Å) with a roughness of about 1.8 Å. In contrast, two surface anions are imaged at the much flatter θ.a termination, thus giving rise to a square-like pattern (2.88 × 2.5-3.2 Å) with a smaller roughness of 1.2 Å. Such a paramount difference between the STM signatures of the two film terminations enables an unambiguous identification of the outer θ.b termination in the experimentally studied films.

The large valence band offset between the oxide film and the NiAl substrate also results in very different binding energies of the Al core electrons. Indeed, XPS experiments systematically reveal Al $2p$ core level shifts (CLS) of 2.5-3.0 eV,[61,61–63] with a much stronger binding of electrons in the oxide. Our results show that the initial state contribution represents about half of this effect and is further enhanced by the final state effects which systematically increase the calculated CLS by an additional 1.5 eV. Figure 9 shows the Al-resolved CLS calculated in the complete screening picture for a variety of alternative configurations in the stoichiometric, O-deficient, and O-rich configurations of alumina bi- and tri-layers in contact with the Al and Ni substrate terminations. (Note that the CLS of Al atoms in the surface layer of the NiAl substrate are less than 1.0 eV and are thus out of the scale in Fig. 9). Apart from Al atoms at either surface or interface θ.b termination, which are characterized by a systematically smaller shift (1.5-2.0 eV), most film cations display CLS values in the 2.0-3.5 eV range, visibly larger than the experimental indications. Focusing more precisely on the 2.5-3.0 eV CLS range (blue stripe in Fig. 9), we find that the stoichiometric θ.ab/Al as well as the O-rich θ.bb/Al and θ.ab/Al configurations match the best the experimental evidence.

Now gathering all complementary information, i.e. the most stable film/interface configurations issued from GO optimization (Fig. 2), the θ.b termination on the external film surface in agreement with STM images, and the mean 2.5-3.0 eV CLS range consistent with XPS measurements, we find that the best overall match between experiments and theory is obtained for the O-rich θ.bb/Al-NiAl bi- (or, possibly, quadri-) layer .

5 Conclusion

We have determined the structural ground states of various ultrathin NiAl(100)-supported alumina films derived from a DFTB-aided genetic algorithm and from the most stable free-standing film structures. Our results clearly demonstrate that θ(100)-like films compete favourably with other polymorphs, such as the dehydrated boehmite, pseudo-$CaIrO_3$, γ, and bixbyite ones, in agreement with existing experimental works. They prove that the θ phase corresponds to the most stable structure on the (2x1)-NiAl substrate not only for stoichiometric films but also for O-poor and O-rich ones, in which the excess or deficiency of oxygen atoms is easily accommodated at the very oxide/metal interface.

Complementing the global optimization simulations, a dedicated DFT analysis reveals that the oxide/metal interaction at stoichiometric interfaces depends surprisingly little on the precise composition of the substrate surface. Conversely, the number of additional/missing Al-O bonds at oxygen-rich/poor interfaces directly drives their relative stability. The present work gives thus insight into the role of the film composition, the nature of its surface and interface terminations, as well as in the mechanisms that stabilize the θ phase, which had not been discussed so far. Finally the comparison between the experimental and theoretical electronic characteristics of the θ-films provides clues on the detailed structure of the experimentally observed films.

6 Acknowledgments

Discussions with Rémi Lazarri, Natalia Alyabyeva, Gregory Cabailh, Jacques Jupille (INSP) and Alexey Koltsov and Jean-Michel Mataigne (ArcelorMittal Maizières Research) are gratefully acknowledged. This work has been supported by French state funds managed by the Agence Nationale de la Recherche as part of the SURFOX project (ANR-16-CE08-0034-01).

7 Conflicts of interest

There are no conflicts to declare

References

1 Y.-F. Sun, S.-B. Liu, F.-L. Meng, J.-Y. Liu, Z. Jin, L.-T. Kong and J.-H. Liu, *Sensors*, 2012, **12**, 2610–2631.

2 K. T. Butler and A. Walsh, *Thin Solid Films*, 2014, **559**, 64–68.

3 A. Dey, *Materials Science and Engineering: B*, 2018, **229**, 206–217.

4 J. S. Park, W.-J. Maeng, H.-S. Kim and J.-S. Park, *Thin Solid Films*, 2012, **520**, 1679–1693.

5 E. Fortunato, P. Barquinha and R. Martins, *Advanced Materials*, 2012, **24**, 2945–2986.

6 M. S. Chen and D. W. Goodman, *Journal of Physics: Condensed Matter*, 2008, **20**, 264013.

7 J. Gustafson, R. Westerström, O. Balmes, A. Resta, R. van Rijn, X. Torrelles, C. T. Herbschleb, J. W. M. Frenken and E. Lundgren, *The Journal of Physical Chemistry C*, 2010, **114**, 4580–4583.

8 S. Shaikhutdinov and H.-J. Freund, *Annual Review of Physical Chemistry*, 2012, **63**, 619–633.

9 Drillet, P., Zermout, Z., Bouleau, D., Mataigne, J. and Claessens, S., *Rev. Met. Paris*, 2004, **101**, 831–837.

10 H.-L. T. Le, J. Goniakowski, C. Noguera, A. Koltsov and J.-M. Mataigne, *The Journal of Physical Chemistry C*, 2017, **121**, 25143–25151.

11 H.-L. T. Le, R. Lazzari, J. Goniakowski, R. Cavallotti, S. Chenot, C. Noguera, J. Jupille, A. Koltsov and J.-M. Mataigne, *The Journal of Physical Chemistry C*, 2017, **121**, 11464–11471.

12 I. Levin and D. Brandon, *Journal of the American Ceramic Society*, 1998, **81**, 1995–2012.

13 J. M. McHale, A. Auroux, A. J. Perrotta and A. Navrotsky, *Science*, 1997, **277**, 788–791.

14 G. Laurens, D. Amans, J. Lam and A.-R. Allouche, *Phys. Rev. B*, 2020, **101**, 045427.

15 M. Van den Bossche, C. Noguera and J. Goniakowski, *Nanoscale*, 2020, **12**, 6153–6163.

16 R. Jaeger, H. Kuhlenbeck, H.-J. Freund, M. Wuttig, W. Hoffmann, R. Franchy and H. Ibach, *Surface Science*, 1991, **259**, 235–252.

17 A. Stierle, F. Renner, R. Streitel, H. Dosch, W. Drube and B. C. Cowie, *Science*, 2004, **303**, 1652–1656.

18 G. Kresse, M. Schmid, E. Napetschnig, M. Shishkin, L. Köhler and P. Varga, *Science*, 2005, **308**, 1440–1442.

19 S. Degen, A. Krupski, M. Kralj, A. Langner, C. Becker, M. Sokolowski and K. Wandelt, *Surface Science*, 2005, **576**, L57–L64.

20 G. Hamm, C. Barth, C. Becker, K. Wandelt and C. R. Henry, *Phys. Rev. Lett.*, 2006, **97**, 126106.

21 M. Schmid, G. Kresse, A. Buchsbaum, E. Napetschnig, S. Gritschneder, M. Reichling and P. Varga, *Phys. Rev. Lett.*, 2007, **99**, 196104.

22 P. Gassmann, R. Franchy and H. Ibach, *Surface Science*, 1994, **319**, 95–109.

23 V. Rose and R. Franchy, *Journal of Applied Physics*, 2009, **105**, 07C902.

24 H. Graupner, L. Hammer, K. Heinz and D. Zehner, *Surface Science*, 1997, **380**, 335–351.

25 Z. Dai, *Institut des NanoSciences de Paris, Paris*, 2017.

26 R.-P. Blum, D. Ahlbehrendt and H. Niehus, *Surface Science*,

1998, **396**, 176–188.
27 A. Stierle, V. Formoso, F. Comin and R. Franchy, *Surface Science*, 2000, **467**, 85–97.
28 N. Frémy, V. Maurice and P. Marcus, *Journal of the American Ceramic Society*, 2003, **86**, 669–75.
29 H. Qin and G. Zhou, *Journal of Applied Physics*, 2013, **114**, 083513.
30 H. Qin, P. Sutter and G. Zhou, *Journal of the American Ceramic Society*, 2014, **97**, 2762–2769.
31 V. Maurice, N. Frémy and P. Marcus, *Surface Science*, 2005, **581**, 88–104.
32 H. Qin, X. Chen, L. Li, P. W. Sutter and G. Zhou, *Proceedings of the National Academy of Sciences*, 2015, **112**, E103–E109.
33 J. P. Pierce and K. F. McCarty, *Phys. Rev. B*, 2005, **71**, 125428.
34 J. P. Pierce, N. C. Bartelt, R. Stumpf and K. F. McCarty, *Phys. Rev. B*, 2008, **77**, 195438.
35 Q. Liu, H. Qin, J. A. Boscoboinik and G. Zhou, *Langmuir*, 2016, **32**, 11414–11421.
36 C. Li, X. Chen, D. Wu, Y. Zhu, H. Qin, J. T. Sadowski and G. Zhou, *Acta Materialia*, 2020, **201**, 244–253.
37 G. Kresse and J. Furthmuller, *Phys. Rev. B*, 1996, **54**, 11169–11186.
38 G. Kresse and J. Hafner, *Phys. Rev. B*, 1993, **47**, 558–561.
39 M. Dion, H. Rydberg, E. Schroder, D. C. Langreth and B. I. Lundqvist, *Phys. Rev. Lett.*, 2004, **92**, 246401.
40 J. Klimes, D. R. Bowler and A. Michaelides, *J. Phys.: Cond. Matt.*, 2010, **22**, 022201.
41 J. Klimes, D. R. Bowler and A. Michaelides, *Phys. Rev. B*, 2011, **83**, 195131.
42 P. E. Blöchl, *Phys. Rev. B*, 1994, **50**, 17953–17979.
43 G. Kresse and J. Joubert, *Phys. Rev. B*, 1999, **59**, 1758–1775.
44 R. F. W. Bader, *Chem. Rev.*, 1991, **91**, 893–928.
45 G. Henkelman, A. Arnaldsson and H. Jonsson, *Comput. Mater. Sci.*, 2006, **36**, 354–360.
46 K. Momma and F. Izumi, *J. Appl. Crystallogr.*, 2011, **41**, 1272–1276.
47 L. Köhler and G. Kresse, *Physical Review B*, 2004, **70**, 165405.
48 V. Nilsson, M. Van den Bossche, A. Hellman and H. Grönbeck, *Surface Science*, 2015, **640**, 59–64.
49 J. Tersoff and D. R. Hamann, *Physical Review B*, 1985, **31**, 805.
50 M. Elstner, D. Porezag, G. Jungnickel, J. Elsner, M. Haugk, T. Frauenheim, S. Suhai and G. Seifert, *Physical Review B*, 1998, **58**, 7260.
51 M. Van den Bossche, *J. Phys. Chem. A*, 2019, **123**, 3038–3045.
52 M. Van den Bossche, H. Grönbeck and B. Hammer, *J. Chem. Theory Comput.*, 2018, **14**, 2797–2807.
53 L. B. Vilhelmsen and B. Hammer, *Physical review letters*, 2012, **108**, 126101.
54 L. B. Vilhelmsen and B. Hammer, *The Journal of chemical physics*, 2014, **141**, 044711.
55 S. R. Bahn and K. W. Jacobsen, *Computing in Science & Engineering*, 2002, **4**, 56–66.
56 A. H. Larsen, J. J. Mortensen, J. Blomqvist, I. E. Castelli, R. Christensen, M. Dułak, J. Friis, M. N. Groves, B. Hammer, C. Hargus *et al.*, *Journal of Physics: Condensed Matter*, 2017, **29**, 273002.
57 D. M. Deaven and K. M. Ho, *Phys. Rev. Lett.*, 1995, **75**, 288–291.
58 L. B. Vilhelmsen and B. Hammer, *The Journal of Chemical Physics*, 2014, **141**, 044711.
59 E. Menéndez-Proupin and G. Gutiérrez, *Physical review B*, 2005, **72**, 035116.
60 J. Goniakowski, F. Finocchi and C. Noguera, *Reports on Progress in Physics*, 2007, **71**, 016501.
61 N. Frémy, V. Maurice and P. Marcus, *Surface and Interface Analysis*, 2002, **34**, 519–523.
62 N. Cai, H. Qin, X. Tong and G. Zhou, *Surface Science*, 2013, **618**, 20–26.
63 N. Cai, Q. Liu, X. Tong and G. Zhou, *Langmuir*, 2014, **30**, 774–783.